

# Counting-loss correction for X-ray spectroscopy using unit impulse pulse shaping

Xu Hong, Jianbin Zhou,\* Shijun Ni, Yingjie Ma, Jianfeng Yao, Wei Zhou, Yi Liu and Min Wang

College of Nuclear Technology and Automation Engineering, Chengdu University of Technology, No.1 the Third Section East, Er Xianqiao Road, Chengdu, Sichuan 610059, People's Republic of China.  
\*Correspondence e-mail: zjb@cdut.edu.cn

Received 19 September 2017

Accepted 5 January 2018

Edited by S. Svensson, Uppsala University, Sweden

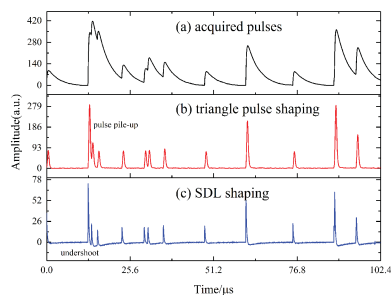
**Keywords:** counting loss correction; X-ray spectroscopy; unit impulse pulse shaping; FAST-SDD detector.

High-precision measurement of X-ray spectra is affected by the statistical fluctuation of the X-ray beam under low-counting-rate conditions. It is also limited by counting loss resulting from the dead-time of the system and pile-up pulse effects, especially in a high-counting-rate environment. In this paper a detection system based on a FAST-SDD detector and a new kind of unit impulse pulse-shaping method is presented, for counting-loss correction in X-ray spectroscopy. The unit impulse pulse-shaping method is evolved by inverse deviation of the pulse from a reset-type preamplifier and a C-R shaper. It is applied to obtain the true incoming rate of the system based on a general fast-slow channel processing model. The pulses in the fast channel are shaped to unit impulse pulse shape which possesses small width and no undershoot. The counting rate in the fast channel is corrected by evaluating the dead-time of the fast channel before it is used to correct the counting loss in the slow channel.

## 1. Introduction

There are many sources of dead-time in radiation measurement systems, including amplifier overload, pile-up rejection, analog-to-digital converter (ADC) and multi-channel analyzer (MCA) store-to-memory (Twomey *et al.*, 1991). Dead-time correction methods are extensively used to correct the counting loss due to dead-time to obtain the true incoming rate. In analog spectroscopy systems, the conversion time of an ADC is regarded as a major source of dead-time and it is often compensated in the counting-loss correction (Roscoe & Furr, 1977; Lindstrom & Fleming, 1995). Counting loss due to pile-up pulse effects is also analyzed and corrected (Bolotin *et al.*, 1970).

With the development of digital radiation spectroscopy, the high-speed ADC has reduced the counting loss due to long conversion time. Also, the application of field programmable gate arrays (FPGAs) and digital signal processing (DSP) improves the digital pulse processing speed, reducing the counting loss coming from analog circuits. Some experiments regarding dead-time in digital spectroscopy systems have already been discussed. For instance, algorithms for pulse shaping and processing were implemented in the DSP code, and  $^{137}\text{Cs}$  spectra were obtained at rates of  $5.9 \times 10^4$  counts  $\text{s}^{-1}$  (CPS) without dead-time (Odell *et al.*, 1999). Moreover, Cardoso *et al.* (2004) analyzed the dead-time in a digital spectrometer through a computational simulation tool, considering the input pulse rate, the existence of pile-up pulse effects and the complexity of algorithms for pulse processing as the primary dead-time sources. In addition, high-speed



ADCs and trapezoidal pulse-shaping algorithms are used by digital pulse processors, such as PX4 and DP5, to eliminate the dead-time associated with peak acquisition and digitization. It is believed that the dead-time in digital spectroscopy is related to pulse shaping (Amptek; <http://amptek.com/>).

In order to create high-precision and high-rate spectra, a general fast–slow channel processing model is established. The slow channel has long shaping time and is used for high-resolution spectra while the fast channel has a short shaping time used for counting-loss correction in the slow channel. Abbene & Gerardi evaluated the dead-time in the fast and slow channel according to the classical dead-time models, paralyzable model and non-paralyzable model (Abbene & Gerardi, 2015; Knoll, 2000). For the low-counting-rate condition, Boromiza *et al.* (2017) made use of the Poisson distribution principle followed by the true counting rate and used the detected counting rate instead of the true counting rate to calculate the correction factor.

In this paper, depending on the fast–slow processing model, the pulses in the fast channel are handled by the unit impulse pulse-shaping method. The true incoming rate is obtained by the corrected counting rate in the fast channel. Also, the pulses in the slow channel are shaped to a trapezoidal pulse with long shaping time.

## 2. Detection system

A structure chart of the detection system is shown in Fig. 1, including a FAST-SDD detector, digital pulse processor (DPP) and PC software. The FAST-SDD detector (XR-

100SDD) is made by Amptek and equipped with a reset-type preamplifier. The energy resolution (full width at half-maximum) of the detector is 125 eV at 5.89 keV peak. The DPP is designed to complete four major tasks: (i) extract the detector output and amplify its amplitude; (ii) convert the analog pulse to a digital pulse for pulse shaping; (iii) shape the sampled pulse with a fast–slow channel processing model; (iv) complete amplitude analysis creating energy spectra and send the spectra data to PC software. The front-end circuit, ADC, FPGA and micro-controller unit (MCU) are integrated to complete the four tasks, respectively.

The front-end circuit, as shown in Fig. 2, is composed of a one-stage C-R shaper and three-stage linear amplifier circuit. The C-R shaper can shape the detector output to an exponential decay pulse shape and the shaping time constant is 3.2  $\mu$ s. The amplitude and offset of the exponential decay pulse are adjustable in the three-stage linear amplifier circuit. Then, the amplified pulse is sampled by the following ADC which is operated at 20 Msp/s (megasamples per second) with 12-bit resolution. The fast–slow channel processing model is realized in the FPGA (Xilinx, XC3S400). The digitized pulse is processed in the fast and slow channel in parallel. Peak detection and counting-loss correction are also accomplished in the FPGA. An STM32F103VET6 chip, which has two serial peripheral interfaces (SPIs) and one CAN interface, is selected as the MCU. The output of the FPGA is transmitted to the MCU by one of the SPI buses, and communication between the MCU and PC software is established by the CAN interface. In addition, the other SPI bus of the MCU is connected to a digital-to-analog convertor (DAC) for amplitude and offset adjustment in the front-end circuit.

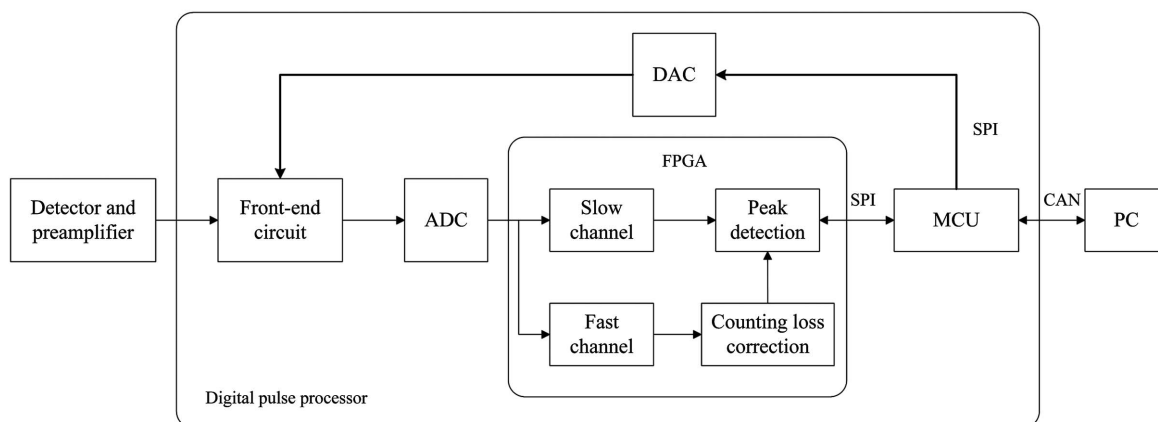


Figure 1 Structure chart of the detection system.

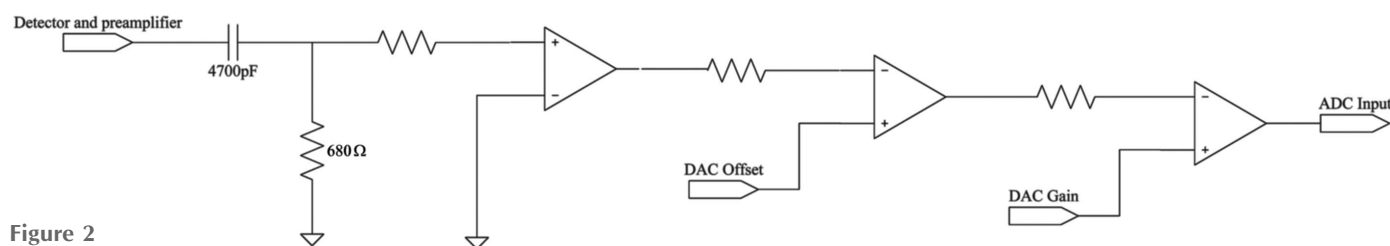
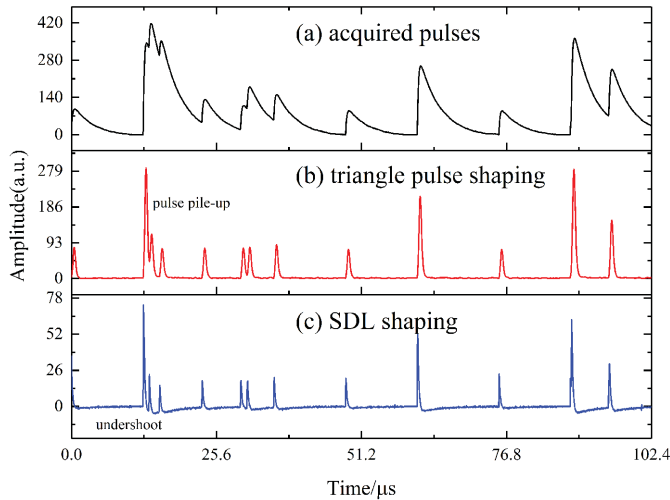


Figure 2 Front-end circuit diagram.



**Figure 3** Triangle pulse shaping and SDL shaping of the acquired pulses from a FAST-SDD. (a) Acquired pulses by ADC. (b) After triangle pulse shaping with 800 ns width. There are pile-up pulses in the shaped pulses. (c) After SDL shaping with one clock cycle delay. The shaped pulses possess undershoot.

In the DPP, the pulse in the slow channel is shaped to a trapezoidal pulse shape, and the pile-up pulse identification technique is also applied to improve the counting rate in the slow channel (Zhou *et al.*, 2015). In order to obtain the true incoming rate, the pulse in the fast channel is usually shaped to a small width by triangle pulse shaping or single delay line (SDL) shaping (Abbene & Gerardi, 2015; Abbene *et al.*, 2010). Fig. 3(a) shows the acquired pulses by ADC. Triangle pulse shaping with 800 ns width and SDL shaping, whose delay time is one clock cycle, are applied to shape the acquired pulses. It can be seen that the shaped pulse after triangle pulse shaping has a relative large width. There are pile-up pulses in the shaped pulses. Although the smaller shaping time can reduce the pulse width, the reduced rising time of the triangle pulse could deteriorate the signal-to-noise ratio. SDL shaping can separate the pile-up pulses in the triangle pulse shaping; however, the shaped pulses possess undershoot.

### 3. Unit impulse pulse shaping

SDL shaping is accomplished by subtracting from the original pulse its delayed and attenuated fraction, and it is easily realized in FPGAs. The width of the shaped pulse is equal to the sum of the delay time and peaking time of the input pulse. In our detection system, the input pulse of SDL shaping is an exponential decay shape, thus there exists undershoot in the shaped pulse. The depth of the undershoot is related to the rising time and falling time of the input pulse.

The exponential decay pulse can be described by

$$y(t) = A[\exp(-t/\tau) - \exp(-t/\theta)], \quad (1)$$

where  $A$  represents the amplitude of the pulse, and  $\tau$  and  $\theta$  are the falling part and rising part, respectively.

Pulses with different values of  $\tau/\theta$  are simulated and the shaped pulses with SDL shaping are illustrated in Fig. 4. It can

be seen that the undershoot depth over pulse amplitude ratio ( $U/A$ ) decreases with increasing  $\tau/\theta$ . The undershoot could be eliminated if  $\tau/\theta$  approaches infinity. It is clear that a step pulse can be taken as an exponential decay pulse with infinite falling time. To be precise, the FAST-SDD detector output is step-shaped.

The processing flow of the detector output is shown in Fig. 5. The unit impulse pulse is generated in the detector after the incident ray is deposited. It is converted to a step pulse after the reset-type preamplifier, and the step pulse is shaped to an exponential decay pulse by the followed C-R shaper. Therefore, only by the reverse process with the C-R shaper and reset-type preamplifier can the unit impulse pulse be obtained. Signal recovery from a C-R shaper and amplifier by deconvolution has been discussed elsewhere (Jordanov, 1994, 2016). In this paper, a realizable algorithm in the FPGA is used to obtain the unit impulse pulse.

#### 3.1. Output of the reset-type preamplifier

The C-R shaper is shown in Fig. 6. According to Kirchhoff's current law, which states that the sum of the current into a junction is equal to the sum of the current out of the junction, the current transmission equation of the circuit can be written as

$$C \frac{d[V_{in}(t) - V_{out}(t)]}{dt} = \frac{V_{out}(t)}{R}. \quad (2)$$

Numerical differentiation can stand for differential operation in equation (2) as the time increment  $dt$  does not approach zero. The differential operation in equation (2) can be written as

$$\begin{aligned} dV_{in}(t) &= V_{in}[n] - V_{in}[n-1] \\ dV_{out}(t) &= V_{out}[n] - V_{out}[n-1] \\ dt &= T_s \end{aligned} \quad (3)$$

where  $V_{out}$  is the ADC output,  $V_{in}$  is the preamplifier output and  $T_s$  is the ADC sampling time.

By substituting equation (3) into equation (2), the recursive relation between  $V_{in}$  and  $V_{out}$  is obtained,

$$V_{in}[n] = (1 + K)V_{out}[n] - V_{out}[n-1] + V_{in}[n-1], \quad (4)$$

where  $K = T_s/(RC)$ .  $RC$  is called the shaping time constant and equals 3.2  $\mu$ s. Assuming that the three-stage linear amplifier circuit only amplifies the pulse amplitude and does not change the shape of the input pulse, the preamplifier output can be recovered by equation (4). Fig. 7(a) shows the digital realization of equation (4) in the FPGA. The sampled pulse is delayed by one clock cycle in the register and is then subtracted from the prompt signal which is amplified  $(1 + K)$  times. The preamplifier output is the addition of the obtained signal and the one-clock-cycle delay.

Fig. 8(a) shows the result of the recovered preamplifier output from a sampled pulse with  $K = 0.015625$ . It indicates that the preamplifier output, which is a step shape, can be recovered by using equation (4).

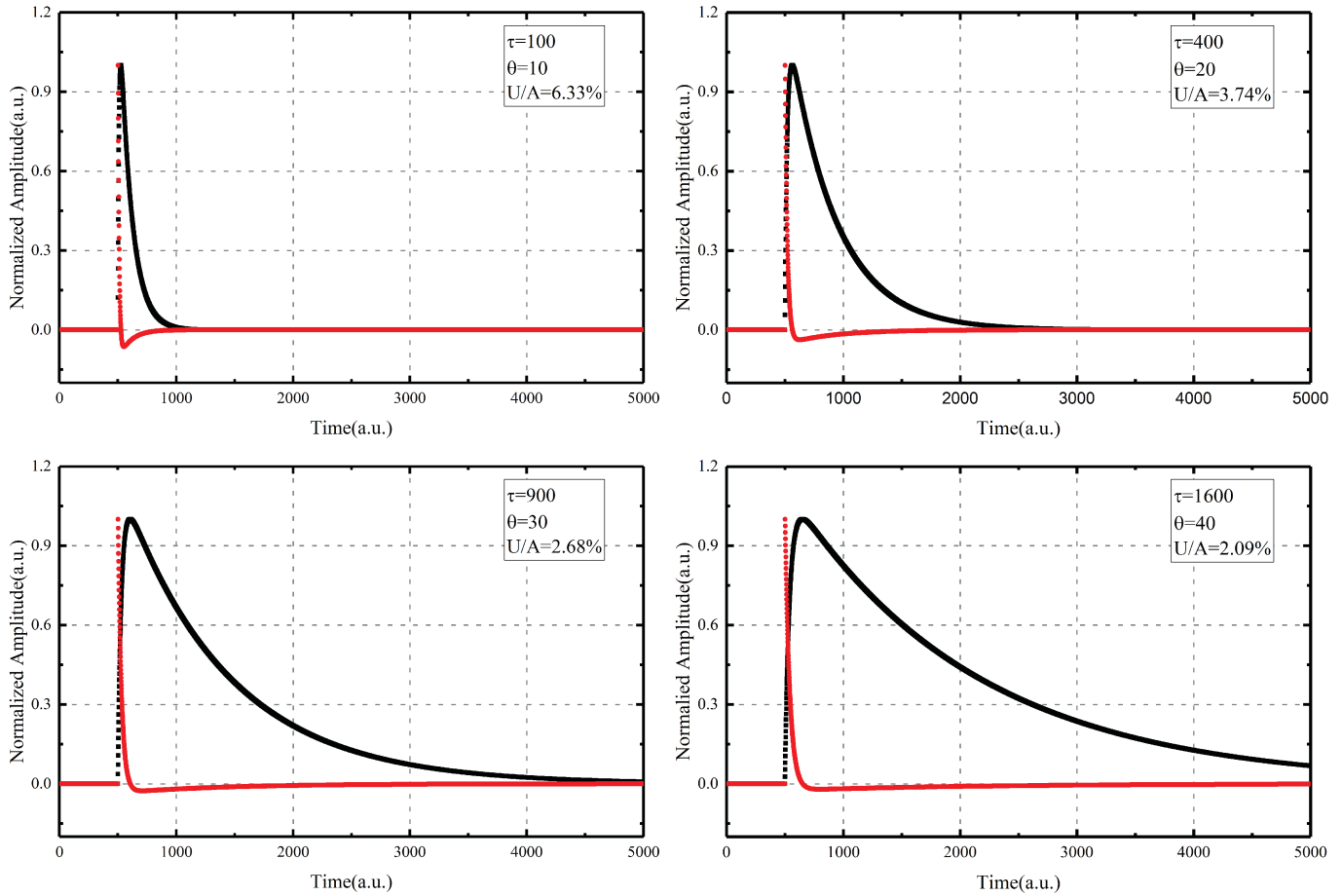


**Figure 4** The ratio of the undershoot depth and pulse amplitude ( $U/A$ ) in SDL shaping decreases with the falling part-to-rising part ratio ( $\tau/\theta$ ) of an exponential decay pulse.

### 3.2. Unit impulse pulse shaping

The response of the incident ray in the detector can be expressed by the unit impulse function  $\delta(t)$ , and the step function  $u(t)$  is used to represent the preamplifier output. The unit impulse function has a differential relation with the step function, as  $\delta(t) = du(t)/dt$ , and the relationship can be described by the following equation in a discrete-time domain,

$$\delta[n] = \frac{u[n] - u[n - 1]}{T_s}. \quad (5)$$

Equation (5) indicates that the unit impulse pulse can be recovered by subtracting the preamplifier output from its one-clock cycle delay. The digital realization of equation (5) is shown in Fig. 7(b). The recovered unit impulse pulse from the step pulse in Fig. 8(a) is pictured in Fig. 8(b).

A conclusion can be drawn that the unit impulse signal in the detector can be obtained from the ADC output in two steps, as equations (4) and (5) stated. Fig. 9 shows the unit

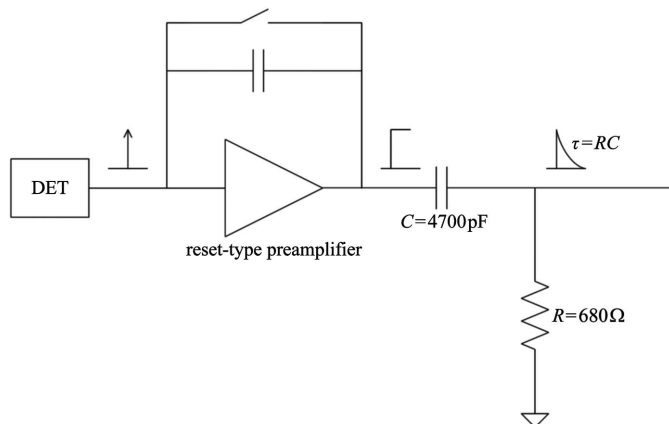


**Figure 5** Processing flow of the detector output.

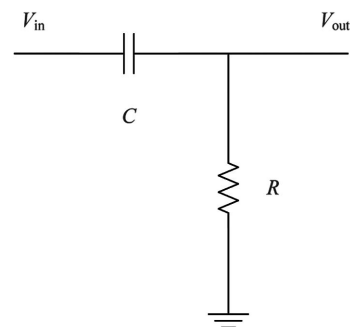


**Figure 6** C-R shaper.

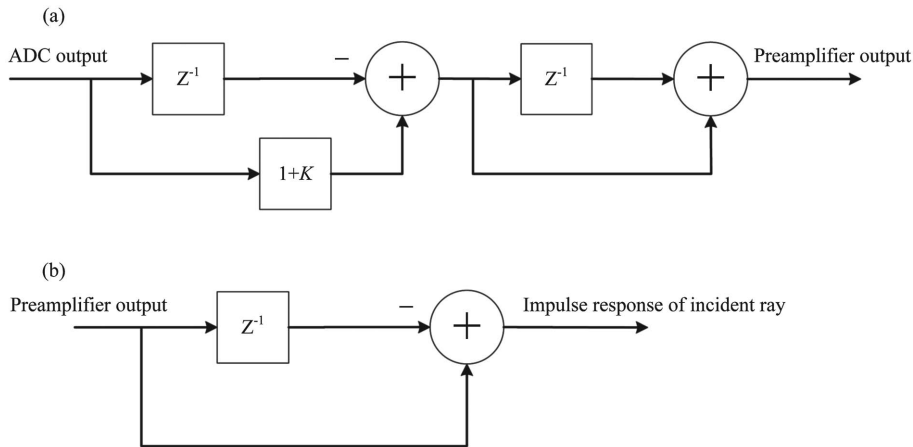


**Figure 7** Digital realization of a unit impulse pulse. (a) Digital realization of the preamplifier output from the ADC output [equation (4)] and (b) digital realization of the unit impulse pulse from the preamplifier output [equation (5)].

impulse pulse-shaping results for the acquired pulses in Fig. 3(a). It can be seen that the undershoot due to SDL shaping is eliminated. Not only is the shaped pulse amplitude unattenuated by the unit impulse pulse shaping but also the pulse width remains unchanged.

## 4. Experimental tests

### 4.1. Dead-time correction in the fast channel

Although the unit impulse pulse has a short width, which is also equal to the sum of the original pulse delay time and its peaking time, the shaped pulse can also be lost due to the

dead-time in the fast channel. The counting rate in the fast channel should be corrected before application. The paralyzable dead-time model and non-paralyzable dead-time models are widely used for dead-time correction (Knoll, 2000).

The time duration  $T$  from starting to process one pulse to being capable of processing another pulse is defined as the dead-time of the radiation system. In the paralyzable model, each arrival event produces a time duration  $T$  and any new arrival event during  $T$  will extend  $T$ . In contrast, the arrival event does not extent  $T$  in the non-paralyzable model. The dead-time models are written as

$$\begin{aligned} m &= n \exp(-nT) && \text{paralyzable model,} \\ m &= n/(1 + nT) && \text{non-paralyzable model,} \end{aligned} \quad (6)$$

where  $m$  represents the detected counting rate and  $n$  is the true incoming rate. These two models describe the behavior of an idealized system; a real system often displays a behavior that is intermediate. The dead-time model in the designed system is paralyzable.

It can be seen from equation (6) that  $n$  cannot be solved explicitly in the paralyzable model. The parameters  $m$  and  $T$  must be achieved primarily. Abbene & Gerardi (2015) established the relation, as shown in equation (7), between the detected counting rate and the X-ray tube current to estimate the dead-time of the fast channel,

$$R_{\text{fast}} = AI \exp(-AIT_{\text{fast}}), \quad (7)$$

where  $A$  is a constant,  $R_{\text{fast}}$ ,  $T_{\text{fast}}$  represent the counting rate and dead-time in the fast channel, respectively, and  $I$  is the X-ray tube current. Equation (7) is similar to the paralyzable model in equation (6). The product of  $A$  and  $I$  stands for the true incoming rate as the number of the generated pulses is proportional to the X-ray tube current with the X-ray tube voltage being constant.

The experiments were carried out by adjusting the X-ray tube current from  $3.9 \mu\text{A}$  to  $70.6 \mu\text{A}$  while the voltage remained constant. The *OriginPro2015* tool was used to construct user-defined relations which conformed to the paralyzable model. The counting rate in the fast channel and its corresponding current is plotted in Fig. 10.  $R_{\text{fast}}$  accords with a positive exponent and the fitting parameter  $R^2 = 0.9999$ . The dead-time

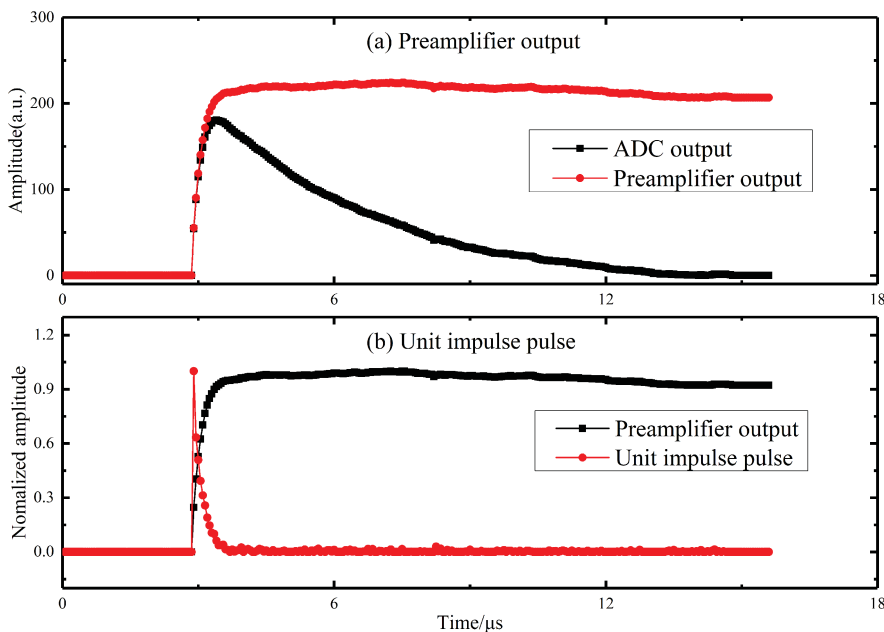


**Figure 8** Recover unit impulse pulse from ADC output. (a) Recover preamplifier output from the ADC output by using equation (4), and (b) recover unit impulse pulse from the preamplifier output by using equation (5).

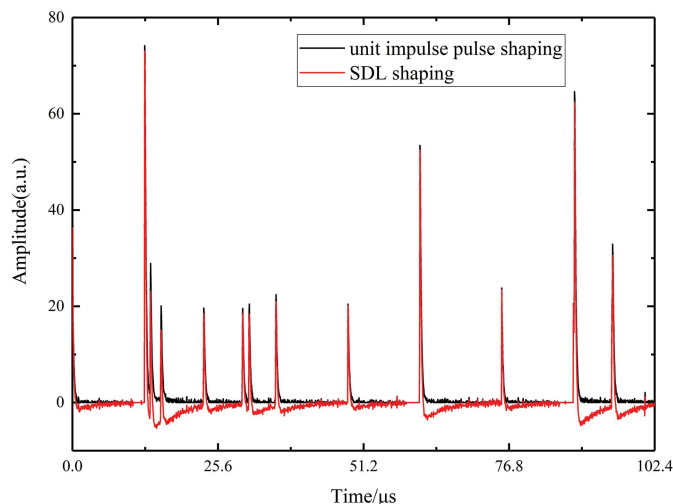


**Figure 9** Unit impulse pulse shaping and SDL shaping of acquired pulses in Fig. 3(a). Unit impulse pulse shaping can eliminate undershoot in the SDL output.

of the fast channel can be calculated as  $T_{fast} = 482$  ns. The availability of the estimated dead-time can also be confirmed in Fig. 8(b) where the shaped pulse width is about 500 ns.

For a low counting rate and small dead-time ( $nT \ll 1$ ), the paralyzable model can be written approximately as the non-paralyzable model, as

$$m = n \exp(-nT) \cong \frac{n}{1 + nT}. \quad (8)$$

Defining the correction factor  $D = n/m$ , equation (8) can be written as

$$D \cong \frac{1}{1 - mT}. \quad (9)$$

Then, the true incoming rate  $R_{true}$  can be obtained from

$$R_{true} = R_{fast} D. \quad (10)$$

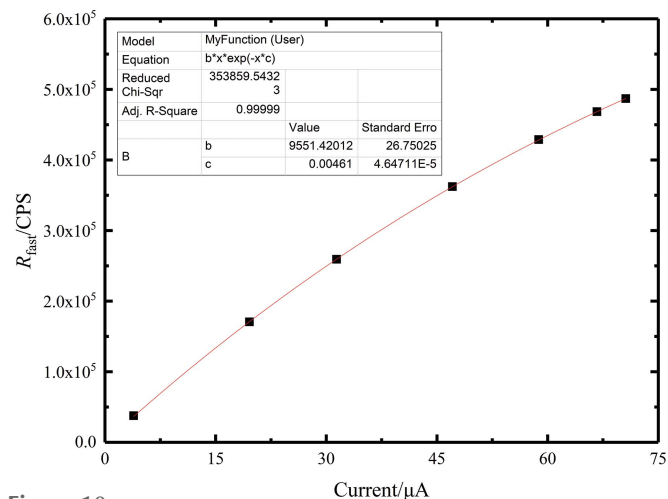


**Figure 10** Measured counting rate by unit impulse pulse shaping in the fast channel (without filter). The good agreement between experimental points and the user-defined relation indicates a paralyzable model.

#### 4.2. Counting-loss correction in the slow channel

The ratio of the true incoming rate  $R_{true}$  and the counting rate from the slow channel  $R_{slow}$  is used to correct the counting loss in the slow channel,

$$R_i = R_{meai}(R_{true}/R_{slow}), \quad (11)$$

where  $R_{meai}$  is the measured counting rate in the  $i$  channel and  $R_i$  is the corrected counting rate.

The X-ray tube (the rated voltage and current are 50 kV and 1 mA) is operated at 49 kV and the current is adjusted, varying from 39.2  $\mu$ A to 784.3  $\mu$ A. The emitting beams are filtered by a combined filter (0.5 mm Ag + 0.5 mm Ag + 0.2 mm Cu) before irradiating a manganese (Mn) sample. The measured counting rates from the fast channel and slow channel are plotted in Fig. 11. Each of the data points is the mean of five measurements. Fig. 11 demonstrates that both the corrected counting rate  $R_{fast}^*$  and  $R_{fast}$  have good linear relation with the current. However, the measured counting rate from the slow channel  $R_{slow}$  tends to decrease because of the increase in the true incoming rate.

Table 1 lists the values of  $R_{fast}$  and  $R_{fast}^*$  and their relative error with the calculated counting rate  $R_{cal}$ .  $R_{cal}$  is obtained according to the proportional relation between the current and the true incoming rate. When the current is 39.2  $\mu$ A, there exists few pile-up pulses and  $R_{fast}$  can be considered as the true incoming rate. Table 1 shows that both  $R_{fast}$  and  $R_{fast}^*$  become closed to  $R_{cal}$  when the counting rate is less than 36.8 kCPS. Therefore, both  $R_{fast}$  and  $R_{fast}^*$  can be applied for the counting-loss correction in the slow channel when the true incoming rate is low (less than 36.8 kCPS).

The filter is removed to study the relation between  $R_{fast}$ ,  $R_{fast}^*$  and the current under high-rate conditions. The recorded values are shown in Fig. 12. In this experiment, with current increases at the initial stage, the counting rate from both the fast channel and slow channel increases. The rate of change of the counting rate is decreased because more and more pile-up

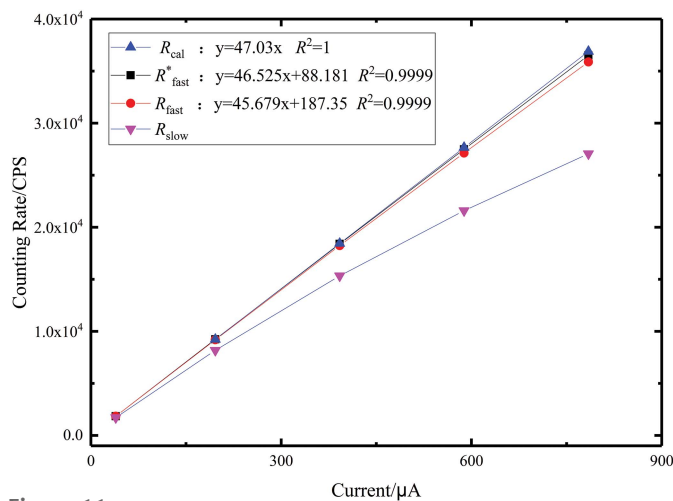


**Figure 11** Measured counting rates in the fast (unit impulse pulse shaping) and slow (trapezoidal pulse shaping) channels (with filter).  $R_{cal}$  is calculated from X-ray tube current. Both  $R_{fast}^*$  and  $R_{fast}$  show excellent linearity versus the X-ray tube current up to 36.8 kCPS.

**Table 1**  
Calculated counting rate and its relative error with  $R_{fast}$  and  $R_{fast}^*$  (with filter).

$I$ ( $\mu\text{A}$ )	$R_{fast}^*$ (CPS)	$R_{fast}$ (CPS)	$R_{slow}$ (CPS)	$R_{cal}$ (CPS)	$(R_{fast}^* - R_{cal})$ $/R_{cal}$	$(R_{fast} - R_{cal})$ $/R_{cal}$	$(R_{slow} - R_{cal})$ $/R_{cal}$
39.2	1845.389	1843.750	1711.663	—	—	—	—
196.1	9237.652	9196.703	8178.763	9222.583	0.16%	-0.28%	-11.32%
392.2	18403.649	18241.833	15337.820	18445.166	-0.23%	-1.10%	-16.85%
588.2	27493.232	27133.663	21594.357	27663.046	-0.61%	-1.91%	-21.94%
784.3	36511.489	35880.053	27057.910	36885.629	-1.01%	-2.73%	-26.64%

**Table 2**  
Calculated counting rate and its relative error with  $R_{fast}$  and  $R_{fast}^*$  (without filter).

$I$ ( $\mu\text{A}$ )	$R_{fast}^*$ (CPS)	$R_{fast}$ (CPS)	$R_{slow}$ (CPS)	$R_{cal}$ (CPS)	$(R_{fast}^* - R_{cal})$ $/R_{cal}$	$(R_{fast} - R_{cal})$ $/R_{cal}$	$(R_{slow} - R_{cal})$ $/R_{cal}$
3.9	38388.768	37691.350	30100.293	—	—	—	—
7.8	75424.281	72778.457	47659.727	75382.700	0.06%	-3.45%	-36.78%
11.8	112207.096	106449.880	58061.480	114040.495	-1.61%	-6.66%	-49.09%
15.7	148913.523	138940.860	64022.320	151731.845	-1.86%	-8.43%	-57.81%
19.6	185930.903	170638.503	67177.113	189423.195	-1.84%	-9.92%	-64.54%
23.5	223075.233	201418.283	68542.543	227114.545	-1.78%	-11.31%	-69.82%
27.5	259798.637	230886.367	68779.103	265772.340	-2.25%	-13.13%	-74.12%
31.4	296293.238	259266.520	68340.993	303463.690	-2.36%	-14.56%	-77.48%
35.3	332324.820	286442.327	67524.070	341155.040	-2.59%	-16.04%	-80.21%
39.2	368190.618	312696.953	66405.357	378846.390	-2.81%	-17.46%	-82.47%
43.1	403939.316	338109.767	65116.777	416537.740	-3.02%	-18.83%	-84.37%
47.1	438867.958	362241.447	63678.710	455195.535	-3.59%	-20.42%	-86.01%
51.0	473084.592	385239.640	62165.340	492886.885	-4.02%	-21.84%	-87.39%
54.9	506960.105	407408.013	60526.780	530578.235	-4.45%	-23.21%	-88.59%
58.8	540562.733	428830.433	58760.973	568269.585	-4.88%	-24.54%	-89.66%
62.7	573221.799	449130.287	56925.487	605960.935	-5.40%	-25.88%	-90.61%
66.7	604961.487	468384.560	55000.977	644618.730	-6.15%	-27.34%	-91.47%
70.6	636152.933	486866.993	52904.16	682310.080	-6.76%	-28.64%	-92.25%

pulses are rejected, especially in the slow channel. The counting rate from the slow channel is significantly less than the counting rate from the fast channel as the current remains increasing. When the current is in excess of 27.5  $\mu\text{A}$ , where  $R_{fast}^* = 259.8$  kCPS,  $R_{slow}$  is in decline. In this situation, a large amount of pile-up pulses are abandoned in the slow channel.

The values of  $R_{fast}$  and  $R_{fast}^*$  and their relative error with  $R_{cal}$  are listed in Table 2. It can be seen that the relative error between  $R_{slow}$  and  $R_{cal}$  increases with the current. It is more than 70% when the current is 27.5  $\mu\text{A}$ . In this case, the calculated counting-rate relative errors with  $R_{fast}^*$  and  $R_{fast}$  are -2.25% and -13.13%, respectively.  $R_{fast}^*$  should be applied for the counting-loss correction in the slow channel instead of  $R_{fast}$ .

The corrected spectra corresponding to the currents 27.5  $\mu\text{A}$ , 39.2  $\mu\text{A}$ , 51.0  $\mu\text{A}$  and 62.7  $\mu\text{A}$  are displayed in Fig. 13. It can be seen that the counting rate in the high-energy region increases with the current. However, the counting rate of the 5.89 keV peak decreases with the current. The spectra in one figure are depicted in Fig. 14. It is shown that the peak position shifts to high energy and the energy resolution is reduced when the current increases. All of these changes in the spectra are caused by the pile-up pulse effects which could enlarge the amplitude of an individual pulse. In conclusion,  $R_{fast}^*$  can be used to correct the counting loss in the slow channel under the condition that the counting rate is within a 265.8 kCPS limit where  $nT = 0.13$ .

### 5. Conclusions

A new kind of unit impulse pulse-shaping method is proposed for pulse shaping in the fast channel. The method is derived based on the reversed analysis of the detector output processing flow, which consists of a reset-type preamplifier and a C-R shaper. The amplitude and width of the shaped pulse are no less than that of the pulse processed with SDL shaping. The presented method can also eliminate under-shoot which exists in SDL output.

The dead-time in the fast channel is estimated by measuring the counting rate with different X-ray tube currents.  $R_{fast}$  is corrected by the estimated dead-time before being used for counting loss correction in the slow channel. For the condition where the incoming rate is less than 36.8 kCPS, both  $R_{fast}$  and  $R_{fast}^*$  have small relative error with  $R_{cal}$ . The quantity of pile-up pulses in the fast channel increases with the X-ray tube current, inducing a counting rate increase in the high-energy region, peak shift and energy resolution deterioration.  $R_{fast}^*$  can be used to correct the counting loss in the slow channel when the incoming rate reaches up to 265.8 kCPS.

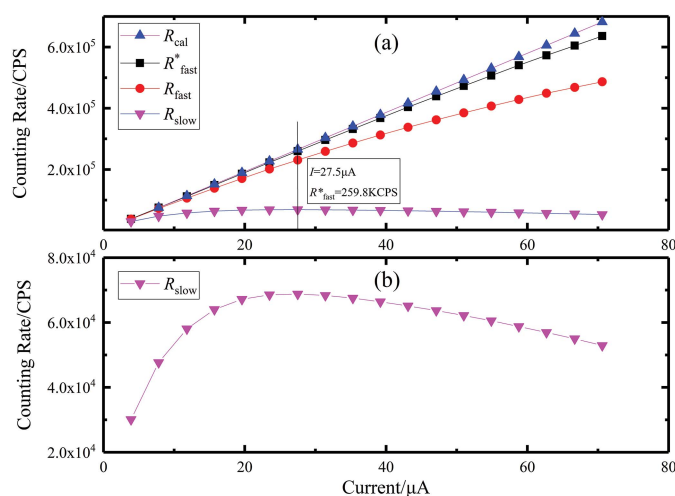


**Figure 12**  
Measured counting rates in the fast (unit impulse pulse shaping) and slow (trapezoidal pulse shaping) channel (without filter). (a) The linearity of  $R_{fast}$  versus current is also deteriorated by the increasing number of pile-up pulses in the fast channel. (b) A large amount of pile-up pulses are abandoned in the slow channel and the measured counting rate decreases when the current goes beyond 27.5  $\mu\text{A}$ .

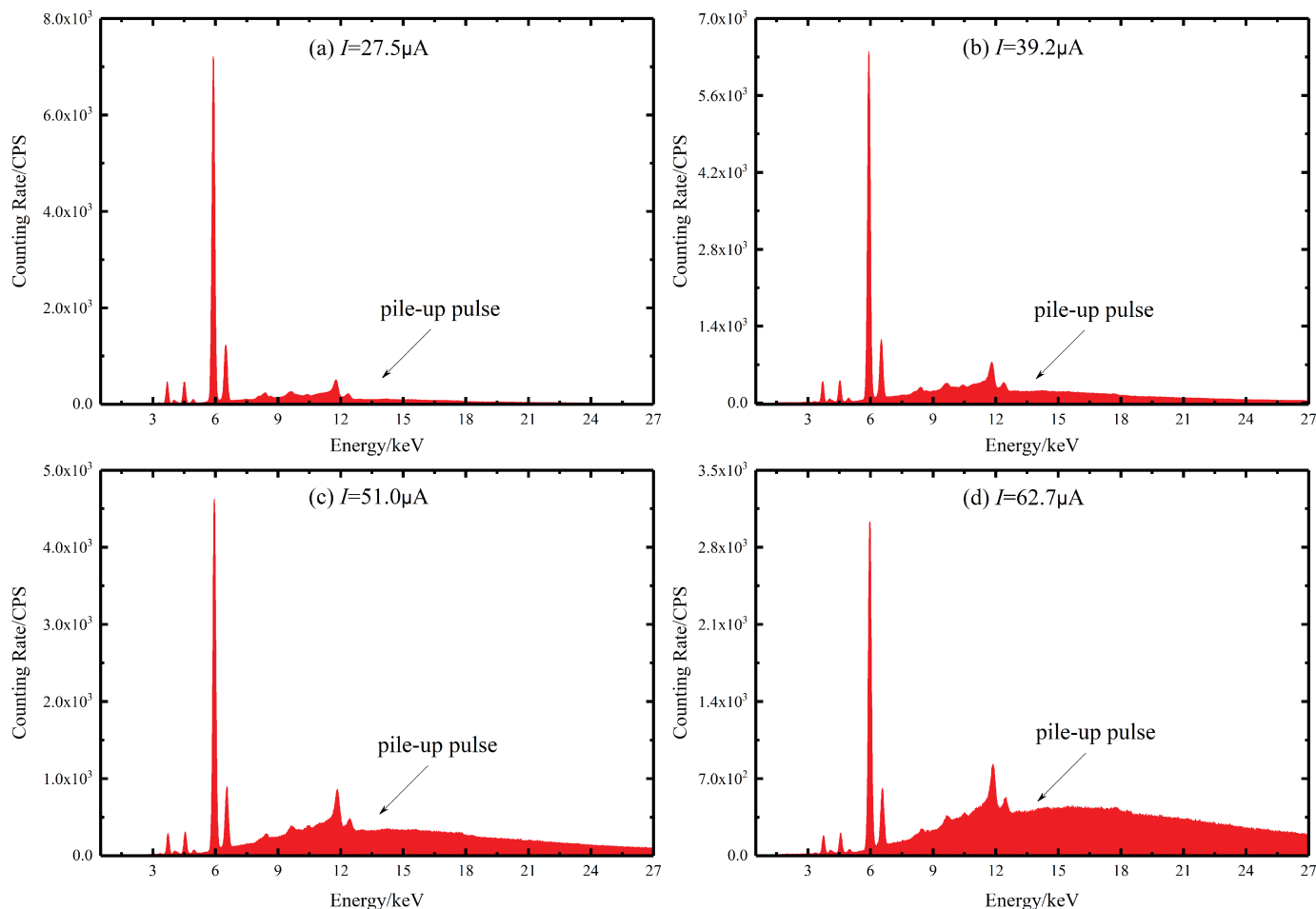


**Figure 13** Corrected spectra with different currents. More and more pile-up pulses are generated as the current increases, and the pile-up pulses result in an increasing counting rate in the high-energy region.

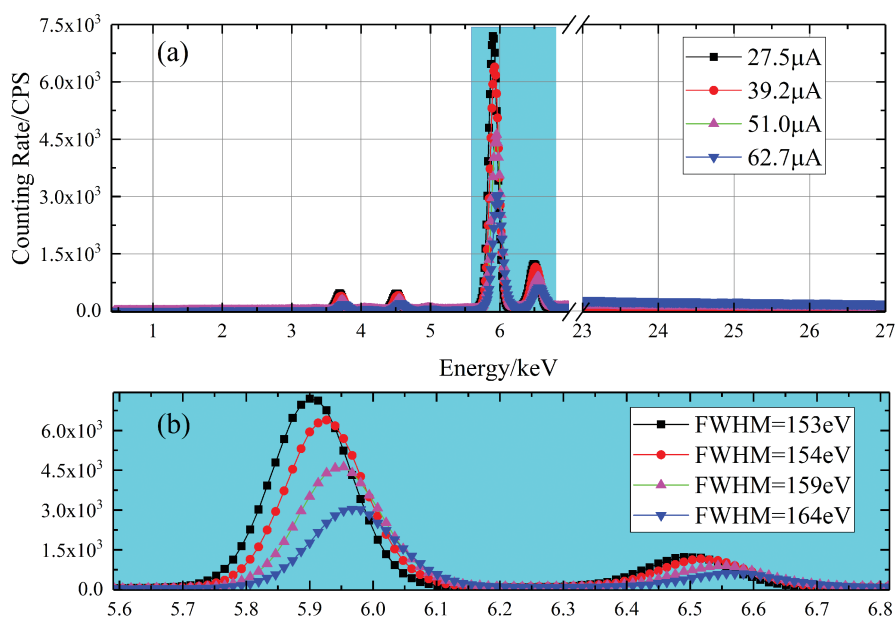


**Figure 14** Pile-up pulse effects cause counting rate decrease and energy resolution deterioration for the 5.89 keV peak. (a) The entire spectra and (b) on an expanded linear scale.

**Funding information**

The following funding is acknowledged: General Program of National Natural Science Foundation of China (grant No. 11475036 to Yingjie Ma); National Key Research and Development Program of China (grant No. 2016YFC1402505 to Jianbin Zhou).

**References**

Abbene, L. & Gerardi, G. (2015). *J. Synchrotron Rad.* **22**, 1190–1201.  
 Abbene, L., Gerardi, G., Principato, F., Del Sordo, S., Ienzi, R. & Raso, G. (2010). *Med. Phys.* **37**, 6147–6156.  
 Bolotin, H. H., Strauss, M. G. & McClure, D. A. (1970). *Nucl. Instrum. Methods*, **88**, 1–12.  
 Boromiza, M., Borcea, C., Negret, A., Olacel, A. & Suliman, G. (2017). *Nucl. Instrum. Methods Phys. Res. A*, **863**, 15–19.  
 Cardoso, J. M., Simões, J. B. & Correia, C. M. B. A. (2004). *Nucl. Instrum. Methods Phys. Res. A*, **522**, 487–494.

- Jordanov, V. T. (1994). *Nucl. Instrum. Methods Phys. Res. A*, **351**, 592–594.
- Jordanov, V. T. (2016). *Nucl. Instrum. Methods Phys. Res. A*, **805**, 63–71.
- Knoll, G. F. (2000). *Radiation Detection and Measurement*, 3rd ed. New York: John Wiley and Sons, Inc.
- Lindstrom, R. M. & Fleming, R. F. (1995). *Radioact. Radiochem.* **6**, 20.
- Odell, D. M. C., Bushart, B. S., Harpring, L. J., Moore, F. S. & Riley, T. N. (1999). *Nucl. Instrum. Methods Phys. Res. A*, **422**, 363–367.
- Roscoe, B. A. & Furr, A. K. (1977). *Nucl. Instrum. Methods*, **140**, 401–404.
- Twomey, T. R., Keyser, R. M., Simpson, M. L. & Wagner, S. E. (1991). *Radioact. Radiochem.* **2**, 1–6.
- Zhou, J.-B., Liu, Y., Hong, X., Zhou, J., Ma, Y.-J., Wang, M., Hu, Y.-C., Chen, B. & Yue, A.-Z. (2015). *Chin. Phys. C* **39**, 068201.